

# Elastoplastic coupling to model cold ceramic powder compaction

S. Stupkiewicz<sup>(1,2)</sup>, A. Piccolroaz<sup>(1)</sup>, and D. Bigoni<sup>(1)</sup>

(1) – Department of Civil, Environmental and Mechanical Engineering,  
University of Trento, via Mesiano 77, I-38123 Trento, Italy

(2) – Institute of Fundamental Technological Research (IPPT),  
Pawinskiego 5B, 02-106 Warsaw, Poland

e-mail: sstupkie@ippt.pan.pl; roaz@ing.unitn.it; bigoni@ing.unitn.it

## Abstract

The simulation of industrial processes involving cold compaction of powders allows for the optimization of the production of both traditional and advanced ceramics. The capabilities of a constitutive model previously proposed by the authors are explored to simulate simple forming processes, both in the small and in the large strain formulation. The model is based on the concept of elastoplastic coupling providing a relation between density changes and variation of elastic properties and has been tailored to describe the transition between a granular ceramic powder and a dense green body. Finite element simulations have been compared with experiments on an alumina ready-to-press powder and an aluminum silicate spray-dried granulate. The simulations show that it is possible to take into account friction at the die wall and to predict the state of residual stress, density distribution and elastic properties in the green body at the end of the forming process.

*Keywords:* Ceramic forming; granular material; elastoplasticity; constitutive model; material modelling

## 1 Introduction

Industrial processes involving the cold forming of ceramic powders can be numerically simulated to detect the distribution of residual stress, density, and elastic properties within the green body, with the purpose of improving design through minimization of defects and regularization of the density distribution. In this way, the industrial production can be enhanced and consequently rejects and energy consumption reduced. Simulations, usually based on the finite element technique, rely on a constitutive model capable of describing the progressive mechanical densification of a granulate. This is a scientific challenge, as it involves the description of the transition between two materials with completely different mechanical behaviour: granular materials are characterized by null cohesion, ‘drop-shaped’ elastic domain, with stress-dependent elastic properties, while green bodies are cohesive, with a ‘cigar-shaped’ elastic domain, characterized by linear elasticity.

Models developed so far are usually<sup>1</sup> variants of known elastoplastic models for soils, based on

---

<sup>1</sup>A remarkable exception is the study by Balakrishnan et al. (2011) has been conducted using discrete element simulations.

the ‘cam clay’ or ‘cap’ yield surfaces (Aydin et al., 1997a, 1997b; Brandt and Nilsson, 1998, 1999; Ewsuk et al., 2001a, 2001b; Gu et al., 2006; Henderson et al. 2000; Keller et al., 1998; Kim et al., 2001; Lee and Kim, 2008; Park and Kim, 2001; Zipse, 1997). In these models the fact that the elastic stiffness of the green body is a function of the density, or in other words of the plastic deformation, (Baklouti et al. 1997; 1999; Carneim et al., 2001; Kim et al., 2002; Kouna Njiwa et al., 2006; Zeuch et al., 2001) is only approximatively kept into account. The key to the rational incorporation of this effect is the concept of elastoplastic coupling, as initiated by Hueckel (1975; 1976) and Dougill (1976), and applied by Piccolroaz et al. (2006a) to the cold densification of ceramic powders, in the form described by Bigoni (2012).

In addition to coupling between plastic and elastic properties, the model developed by Piccolroaz et al. (2006a), incorporates micromechanically-based hardening laws and a previously-defined yield function, called in the following ‘BP’ (Bigoni and Piccolroaz, 2004; Piccolroaz and Bigoni, 2009; Bigoni, 2012). This yield function possesses the ‘high stretchability’ needed to describe the granular/solid transition typical of ceramics forming, but has the inconvenience that it is defined infinity outside the elastic domain. This inconvenience, preventing the use of standard implicit return mapping schemes for integration of rate constitutive equations, has been recently overcome in different ways (Brannon and Leelavanichkul, 2010; Penasa et al., 2013; Stupkiewicz et al., 2013), so that the model is currently ready to be used. In particular, computer implementation has been carried out using the automatic code generation system *AceGen*, and the computations have been performed using the finite element package *AceFEM* (Korelc, 2002; 2009).

The purpose of the present article is to demonstrate, through a new implementation allowing us to introduce large strain and friction at the mould/granulate interface, the capabilities of the above-described model in simulating forming processes of both advanced (a ready-to-press alumina) and traditional (an aluminum silicate spray-dried granulate) ceramic powders. To this end, examples of computations are presented and compared to experiments for uniaxial strain, single and double action pressing into a mould with friction at the walls and forming with a cross-shaped punch. The comparison with experiments shows the excellent capability of the model, particularly in the large strain version, to simulate the mechanical features of cold forming of ceramic powders.

## 2 The concept of elastoplastic coupling

The force vs. displacement relation (with unloadings) for the uniaxial strain of aluminum silicate spray-dried granulate (6 g powder pressed in a 25 mm diameter mould), reported in Fig. 1, shows well-known mechanical features of cold powder compaction: (i.) the large plastic (i.e. irreversible) deformation and (ii.) the progressive elastic stiffening of the material, related to the increase of density.

These two features are key aspects in the modelling and can be incorporated in a constitutive law in a rigorous way through the notion of elastoplastic coupling. In this section we illustrate this concept with reference to a simple small-strain model.<sup>2</sup>

In particular, the deformation  $\epsilon$  is assumed to be the sum of a plastic,  $\epsilon_p$ , and an elastic,  $\epsilon_e$ ,

---

<sup>2</sup>For a comprehensive description of elastoplastic coupling in both small-strain and finite-strain formulations, the interested reader is referred to Piccolroaz et al. (2006a, 2006b), Bigoni (2012).

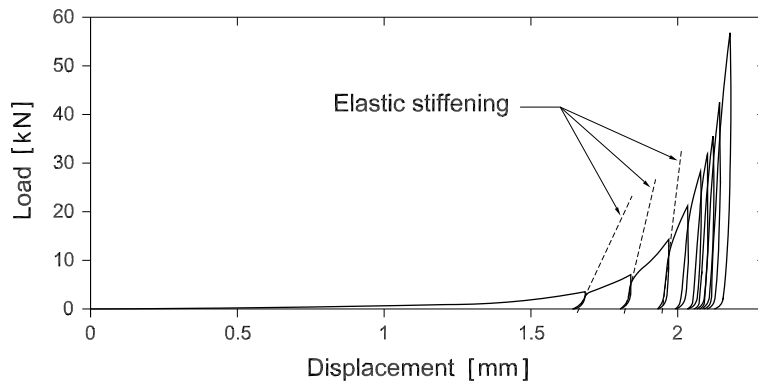


Figure 1: Uniaxial deformation of an aluminum silicate spray-dried powder (force versus displacement) with un-loadings, showing the progressive stiffening of the material.

component, namely,

$$\epsilon = \epsilon_e + \epsilon_p, \quad (2.1)$$

where the elastic deformation is induced by the stress  $\sigma$ , but, due to elastoplastic coupling, is also function of the plastic deformation

$$\epsilon_e = \hat{\epsilon}_e(\sigma, \epsilon_p), \quad (2.2)$$

so that

$$\epsilon = \hat{\epsilon}_e(\sigma, \epsilon_p) + \epsilon_p. \quad (2.3)$$

As a response to stress and plastic strain increments,  $\dot{\sigma}$  and  $\dot{\epsilon}_p$ , the strain is incremented as

$$\dot{\epsilon} = \frac{\partial \hat{\epsilon}_e(\sigma, \epsilon_p)}{\partial \sigma} \dot{\sigma} + \underbrace{\frac{\partial \hat{\epsilon}_e(\sigma, \epsilon_p)}{\partial \epsilon_p}}_{e-p \text{ coupling}} \dot{\epsilon}_p + \dot{\epsilon}_p, \quad (2.4)$$

explicitly showing the elastoplastic coupling term, absent in the usual theories of elastoplasticity, as for instance the Cam-clay.

To elucidate with a simple example the elastoplastic coupled formulation, we refer to the Cooper and Eaton (1962) isostatic compaction model, in which the plastic volumetric strain  $e_v^p$  is related to the hydrostatic compaction pressure  $p_c$  as

$$e_v^p = -\tilde{a}_1 \exp\left(-\frac{\Lambda_1}{p_c}\right) - \tilde{a}_2 \exp\left(-\frac{\Lambda_2}{p_c}\right), \quad (2.5)$$

where, for the aluminum silicate powder reported in Fig. 1, the constants assume the following values:  $\tilde{a}_1=0.5$ ,  $\tilde{a}_2=0.05$ ,  $\Lambda_1=0.96$ , and  $\Lambda_2=40.6$ . For the sake of simplicity the following elastic law is adopted

$$e_v^e = p_c/B(e_v^p), \quad (2.6)$$

defined by the elastic bulk modulus  $B(e_v^p)$ , exponential function of the plastic volumetric deformation

$$B(e_v^p) = B^\infty - (B^\infty - B^0) \exp(-\alpha|e_v^p|), \quad (2.7)$$

which can be viewed as a simplification of the law reported by Kim et al. 2002. The constants  $B^\infty$  and  $B^0$  assume, for the aluminum silicate powder, the values 4 GPa and 50 KPa, respectively.

Identifying now in eqn (2.3) the strain variable with the volumetric strain  $e_v$  and the stress variable with  $p_c$  we obtain

$$e_v = \frac{p_c}{B(e_v^p)} + e_v^p. \quad (2.8)$$

Eq (2.8) describes an isostatic forming process for an aluminum silicate granulate and has been plotted in Fig. 2, which clearly shows the effect of the elastoplastic coupling, namely, an increase of the elastic stiffness with the increase of the plastic deformation. Note that the model is simple, so that hysteresis of the unloading-reloading behaviour (visible in Fig. 1) is not described.

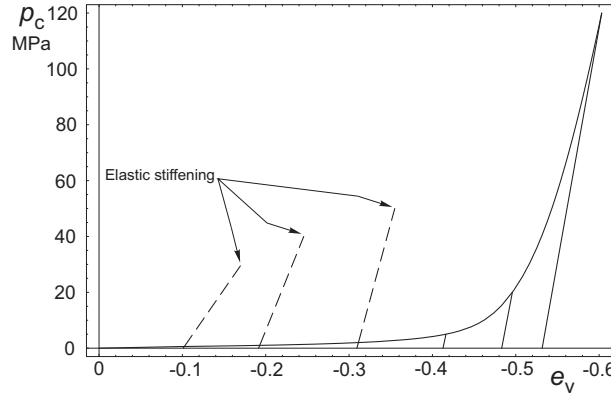


Figure 2: Simulated isostatic forming, eq (2.8), of an aluminum silicate granulate (compacting pressure versus volumetric deformation) with unloadings, showing the progressive stiffening of the material due to elastoplastic coupling.

As an alternative to the compliance approach, eq (2.2), a stiffness approach can equivalently be pursued in which the stress is assumed to be a function of the elastic and plastic strain

$$\sigma = \hat{\sigma}(\epsilon_e, \epsilon_p), \quad (2.9)$$

so that, as a response to a strain increment  $\dot{\epsilon}$ , the stress is incremented as

$$\dot{\sigma} = \frac{\partial \hat{\sigma}(\epsilon_e, \epsilon_p)}{\partial \epsilon_e} \dot{\epsilon}_e + \frac{\partial \hat{\sigma}(\epsilon_e, \epsilon_p)}{\partial \epsilon_p} \dot{\epsilon}_p, \quad (2.10)$$

which, using eq (2.1), can be rewritten in a way which explicitly shows the elastoplastic coupling term

$$\dot{\sigma} = \frac{\partial \hat{\sigma}(\epsilon_e, \epsilon_p)}{\partial \epsilon_e} \dot{\epsilon} - \underbrace{\frac{\partial \hat{\sigma}(\epsilon_e, \epsilon_p)}{\partial \epsilon_e} \dot{\epsilon}_p + \frac{\partial \hat{\sigma}(\epsilon_e, \epsilon_p)}{\partial \epsilon_p} \dot{\epsilon}_p}_{e-p \text{ coupling}}. \quad (2.11)$$

The equivalence of the two formulations (2.4) and (2.11) can be shown through a substitution of eq (2.2) into eq (2.9) to obtain the identity

$$\epsilon_e = \hat{\epsilon}_e(\hat{\sigma}(\epsilon_e, \epsilon_p), \epsilon_p), \quad (2.12)$$



which differentiated gives

$$\frac{\partial \hat{\epsilon}_e}{\partial \hat{\sigma}} \frac{\partial \hat{\sigma}}{\partial \hat{\epsilon}_e} = 1, \quad - \frac{\partial \hat{\epsilon}_e}{\partial \hat{\sigma}} \frac{\partial \hat{\sigma}}{\partial \epsilon_p} = \frac{\partial \hat{\epsilon}_e}{\partial \epsilon_p}, \quad (2.13)$$

allowing the transformation of eq (2.4) into eq (2.11) and viceversa.

The elastoplastic model developed by Piccolroaz et al. (2006a) for the forming of ceramic powders is based on a stiffness formulation of elastoplastic coupling as that given by eq (2.11), where, to enforce hyperelasticity, the stress

$$\begin{aligned} \boldsymbol{\sigma}(\boldsymbol{\epsilon}_e, e_v^p) = & \left\{ -\frac{2}{3}\mu e_v^e + c \right. \\ & \left. + (p_0 + c) \left[ \left( d(e_v^p) - \frac{1}{d(e_v^p)} \right) \frac{e_v^e}{\tilde{\kappa}} - \exp \left( -\frac{e_v^e}{d(e_v^p)^{1/n} \tilde{\kappa}} \right) \right] \right\} \mathbf{I} + 2\mu \boldsymbol{\epsilon}^e, \end{aligned} \quad (2.14)$$

(note that  $e_v^e = \text{tr} \boldsymbol{\epsilon}^e$  and  $e_v^p = \text{tr} \boldsymbol{\epsilon}^p$  are respectively the elastic and the plastic volumetric strains) is obtained as the gradient of the following elastic potential

$$\begin{aligned} \phi(\boldsymbol{\epsilon}^e, e_v^p) = & -\frac{\mu(d)}{3} (e_v^e)^2 + c e_v^e \\ & + (p_0 + c) \left[ \left( d - \frac{1}{d} \right) \frac{(e_v^e)^2}{2\tilde{\kappa}} + d^{1/n} \tilde{\kappa} \exp \left( -\frac{e_v^e}{d^{1/n} \tilde{\kappa}} \right) \right] + \mu(d) \boldsymbol{\epsilon}^e \cdot \boldsymbol{\epsilon}^e. \end{aligned} \quad (2.15)$$

In eqs (2.14) and (2.15), the parameter  $d(e_v^p) \geq 1$  describes the transition between the logarithmic nonlinear elasticity, typical of granular material (occurring when  $d = 1$ ), and the elastic law with stiffness linearly increasing with the forming pressure, typical of the dense green body (occurring when  $d \rightarrow \infty$ ). In particular, parameter  $d$  is assumed to be a linear function of forming pressure  $p_c$ , for values of pressure superior to the breakpoint threshold  $p_{cb}$ , namely,

$$d = 1 + B \langle p_c - p_{cb} \rangle, \quad (2.16)$$

where  $B$  is a positive material parameter and the symbol  $\langle \rangle$  denotes the Macaulay brackets.

In eqs (2.14) and (2.15)  $\tilde{\kappa}$  is a modification of the logarithmic bulk modulus of the powder, modified through the initial void ratio  $e_0$  (at which the mean stress  $p$  is equal to  $p_0$ ) as

$$\tilde{\kappa} = \kappa / (1 + e_0), \quad (2.17)$$

$c$  is the cohesion (null in the initial phase of loose granulate), evolving with the following hardening law

$$c = c_\infty [1 - \exp(-\Gamma \langle p_c - p_{cb} \rangle)], \quad (2.18)$$

where  $p_{cb}$  is the breakpoint pressure,  $c_\infty$  and  $\Gamma$  are two positive material parameters, the former defining the limit value of cohesion reached after large plastic deformation, the latter related to the ‘velocity of growth’ of cohesion. Finally, the elastic shear modulus  $\mu$  is taken in eqs (2.14) and (2.15) to depend on the plastic volumetric strain through the coupling parameter  $d$  and the cohesion  $c$  as follows

$$\mu(d) = \mu_0 + c \left( d - \frac{1}{d} \right) \mu_1, \quad (2.19)$$

where  $\mu_0$ , and  $\mu_1$  are positive material constants.

The final, but essential, ingredient in the modelling of cold powder compaction is the yield surface, defining the stress locus corresponding to the elastic range, which in the form introduced by Bigoni and Piccolroaz (2004) is given by

$$f(p, p_c, c) + \frac{q}{g(\theta)} = 0, \quad (2.20)$$

where  $q = \sqrt{3\boldsymbol{\sigma} \cdot \boldsymbol{\sigma}/2 - \text{tr}^2\boldsymbol{\sigma}/2}$  is the second deviatoric invariant,  $f(p, p_c, c)$  is the function defining the dependence on the mean pressure  $p = -\text{tr}\boldsymbol{\sigma}/3$ , namely,

$$f(p, p_c, c) = -Mp_c \sqrt{\left[ \frac{p+c}{p_c+c} - \left( \frac{p+c}{p_c+c} \right)^m \right] \left[ 2(1-\alpha) \frac{p+c}{p_c+c} + \alpha \right]}, \quad (2.21)$$

and  $g(\theta)$  describes dependence on the Lode's invariant  $\theta$ , assumed in the form

$$g(\theta) = \frac{1}{\cos \left[ \beta \frac{\pi}{6} - \frac{1}{3} \cos^{-1} (\gamma \cos 3\theta) \right]}. \quad (2.22)$$

The shape of the yield surface depends on the six parameters  $\alpha, M, p_c, c, \beta, \gamma$  and is extremely flexible and thus capable of describing the yield locus of many different materials. The yield surfaces for the ready-to-press alumina and for the aluminum silicate granulate employed in the present article are shown in Fig. 3.

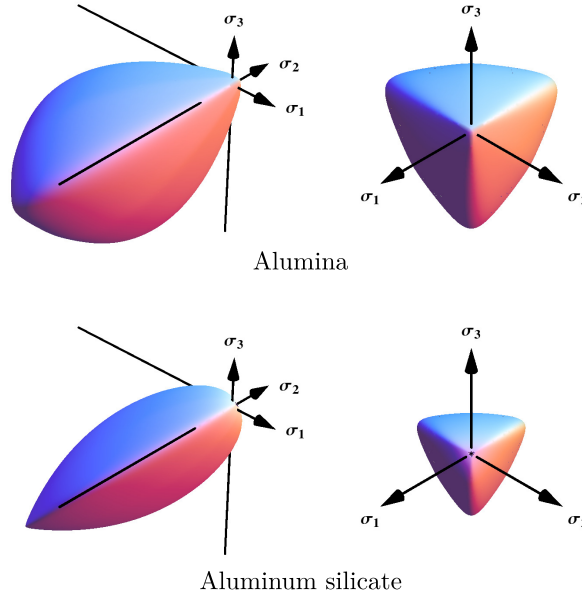


Figure 3: The BP yield surfaces with the parameters suited to model the ready-to-press alumina powder and the aluminum silicate granulate employed in the present article.

The described elastoplastic coupled model has been also produced in a large strain version by Piccolroaz et al. (2006b). Both the small and the large strain versions of the model have been implemented in a finite element program and will be employed in the next section to assess their predictive capabilities.

### 3 Numerical simulations versus experimental results

Simulations of cold compaction processes are presented in this section with reference to:

- the ready-to-press 392 Martoxid KMS-96 alumina powder characterized by the constitutive parameters identified by Piccolroaz et al. (2006a, their Table 1), with the slight modifications reported below;
- the aluminum silicate spray-dried powder (used in the production of tiles) experimentally characterized by Bosi et al. (2013).

The simulations, performed with the small and the large strain versions of the elastoplastic coupled model presented in the previous section, refer to uniaxial deformation, single and double action compaction in a mould with friction at the powder/wall contact, and forming into a mould with a cross-shaped punch, designed by us to induce a strong variation in the mechanical properties after forming. In all cases the simulations have been compared to experimental results, some already available (Piccolroaz et al. 2006a; Bosi et al., 2013) and other performed for the present study.

In order to enable direct comparison of the small and the large strain models, the constitutive parameters adopted for the alumina powder have been slightly modified with respect to the values reported by Piccolroaz et al. (2006a) so that the uniaxial response of the two models is as close as possible. This is illustrated in Section 3.1. Specifically, parameter  $B$  has been set to  $B = 0.6 \text{ MPa}^{-1}$  in the small strain model and to  $B = 0.18 \text{ MPa}^{-1}$  in the finite strain model, while parameters  $\tilde{a}_1$  and  $\tilde{a}_2$  have been set to  $\tilde{a}_1 = 0.383$  and  $\tilde{a}_2 = 0.124$  for both models (compared to the original values of 0.37 and 0.12, respectively). Further, parameter  $\epsilon$  defining the flow rule non-associativity has been set to  $\epsilon = 0.5$ . In the case of the aluminum silicate powder, the parameter  $M$  of the yield surface has been increased to 0.5 with respect to the value reported by Bosi et al. (2013) to avoid near-boundary numerical instabilities. Material parameters of the models employed for the finite strain simulations are summarized in Table 1, where  $\rho_T$  is the theoretical density of the powder.

The present finite element implementation of the model, with full account for the elastoplastic coupling, employs the standard return mapping algorithm combined with the implicit backward-Euler time integration scheme. The difficulties associated with the application of the return mapping algorithm to the BP yield surface have been overcome in different ways, one reported by Penasa et al. (2013), and the other used here is based on the concept of implicit yield surface that is described by Stupkiewicz et al. (2013). The computer implementation has been carried out using the automatic code generation system *AceGen* (Korelc, 2002; 2009). In particular, the automatic differentiation technique implemented in *AceGen* has been applied to derive the consistent tangent matrix. Exact linearization of the incremental constitutive relationships is crucial for the convergence of the Newton method used to solve the nonlinear finite element equations.

The example studied in Section 3.2 involves frictional contact interaction of the ceramic powder sample with the mould and the punch. Efficient and robust treatment of the corresponding uni-

Yield surface	$M$	$m$	$\alpha$	$\beta$	$\gamma$
Alumina	1.1	2	0.1	0.19	0.9
Aluminum silicate	0.5	4.38	1.95	0.1	0.9
Elastic log. bulk mod.	$\kappa$		Flow rule	$\epsilon$	
Alumina	0.04			0.5	
Aluminum silicate	0.08			0.5	
1st hardening law	$\tilde{a}_1$	$\tilde{a}_2$	$\Lambda_1$	$\Lambda_2$	
Alumina	0.383	0.124	1.8 MPa	40 MPa	
Aluminum silicate	0.497	0.057	1.14 MPa	40.9 MPa	
2nd hardening law	$c_\infty$	$\Gamma$	$p_{cb}$		
Alumina	2.3 MPa	0.026 MPa <sup>-1</sup>	3.2 MPa		
Aluminum silicate	0.778 MPa	0.046 MPa <sup>-1</sup>	1.3 MPa		
E-P coupling	$B$	$n$	$\mu_0$	$\mu_1$	
Alumina	0.18 MPa <sup>-1</sup>	6	1 MPa	64	
Aluminum silicate	2.16 MPa <sup>-1</sup>	6	1 MPa	16	
Initial state	$e_0$	$p_0$	$\rho_T$		
Alumina	2.129	0.063 MPa	3.98 g/cm <sup>3</sup>		
Aluminum silicate	1.741	0.09 MPa	2.60 g/cm <sup>3</sup>		

Table 1: Material parameters used for finite strain simulations.

lateral contact and friction constraints relies on application of the augmented Lagrangian method of Alart and Curnier (1991), see also Lengiewicz et al. (2011) for the details of the computer implementation.

### 3.1 Uniaxial strain of ceramic powder

Simulations of uniaxial strain of alumina powder are reported and compared to experimental results in Fig. 4. The results are reported in terms of force versus displacement relations and referred to four 30 mm diameter cylindrical specimens of the nominal initial height of 8.7 mm compacted to 60, 80, 100 and 120 MPa and subsequently unloaded. The actual initial height of the specimens was 8.73, 8.64, 8.78 and 8.66 mm, respectively.

Simulations show an excellent agreement with experimental results, particularly for the large strain analyses. As discussed above, the constitutive parameters of the small and the large strain models have been adopted such that the uniaxial response of the two models is as close as possible. The two responses are indeed very close except in an intermediate range of small compaction pressures where a small difference is observed, see Fig. 4.

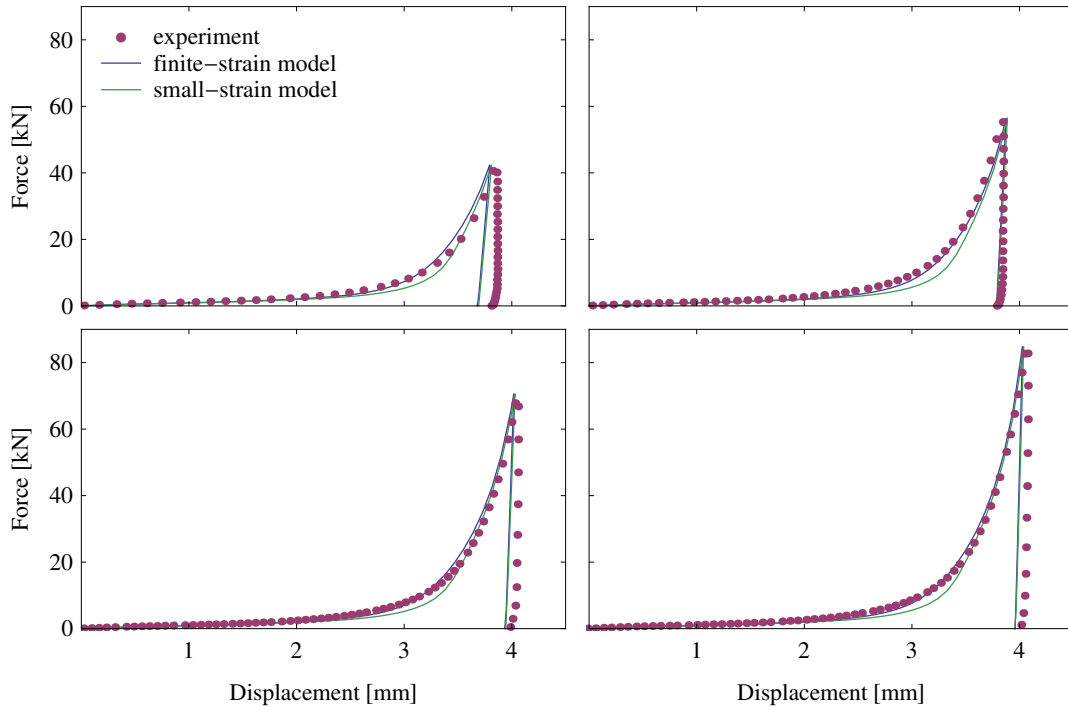


Figure 4: Uniaxial strain of alumina: small-strain and finite-strain models compared to the experiment of Piccolroaz et al. (2006a). Upper part: compaction at 60MPa (left) and at 80MPa (right). Lower part: compaction at 100MPa (left) and at 120MPa (right).

### 3.2 Single and double action forming into a mould with wall friction: density distribution

We simulate single and double action cold compression of ceramic powder into a (38.2 mm diameter) cylindrical rigid mould in the presence of Coulomb friction between the powder and the mould wall, with the friction coefficient equal to 0.4. Samples of alumina and aluminum silicate have been analyzed with an initial height of 113.9 mm and 128.5 mm, respectively. Numerical simulation (to mimic the experimental procedure) has been performed providing first a frictionless preforming uniaxial strain corresponding to a compression of 3 MPa and later providing the final forming pressure of 40 MPa in the presence of friction. The problem is treated as axisymmetric.

Undeformed and deformed (after loading, subsequent unloading, and ejection from the mould) meshes are reported in Fig. 5 for single action and double action compression of alumina powder. In addition to the nonuniform mesh distortion induced by friction at the wall, we can note from Fig. 5 the better compaction reached with double action, leading to a final height smaller than that obtained with the single action compression.

The distributions of density, cohesion and tangent elastic bulk modulus are shown in Fig. 6 for single (upper part) and double (lower part) action compression. This figure clearly shows that density, cohesion and elastic properties obtained at the end of the forming process are much more

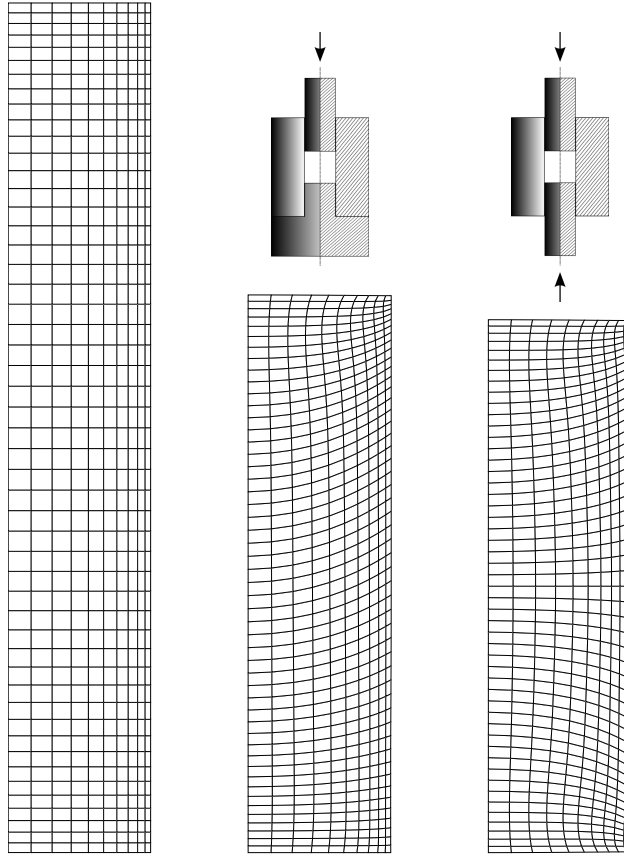


Figure 5: Finite element mesh for single and double action forming of alumina powder with friction (coefficient has been assumed equal to 0.4) at the mould wall. From left to right: undeformed, deformed for single action compression, and for double action compression.

uniform with the double action device than with the single action.

Finally, the density distribution (averaged through the cross section of the sample) along the height of the sample, simulated for the alumina and the aluminum silicate powder, are reported in Fig. 7 and compared with experimental results. Experiments have been performed by subsequently charging a mould with powder and compressing at 3 MPa, so that to obtain a ‘layered’ sample, to be finally loaded at 40 MPa. Due to the small height of the ‘layering’, the influence of friction was negligible during the compression at 3 MPa, but friction was important during compaction at 40 MPa.

Note that experiments for the single action compression were not performed on the alumina sample (so that these are not reported in Fig. 7). The simulated density distributions are in good qualitative and quantitative agreement with experimental results, with a discrepancy partly due to the fact that the double action compression was simulated assuming perfectly symmetric action of the two punches while this symmetry was not exactly preserved in the experiment.

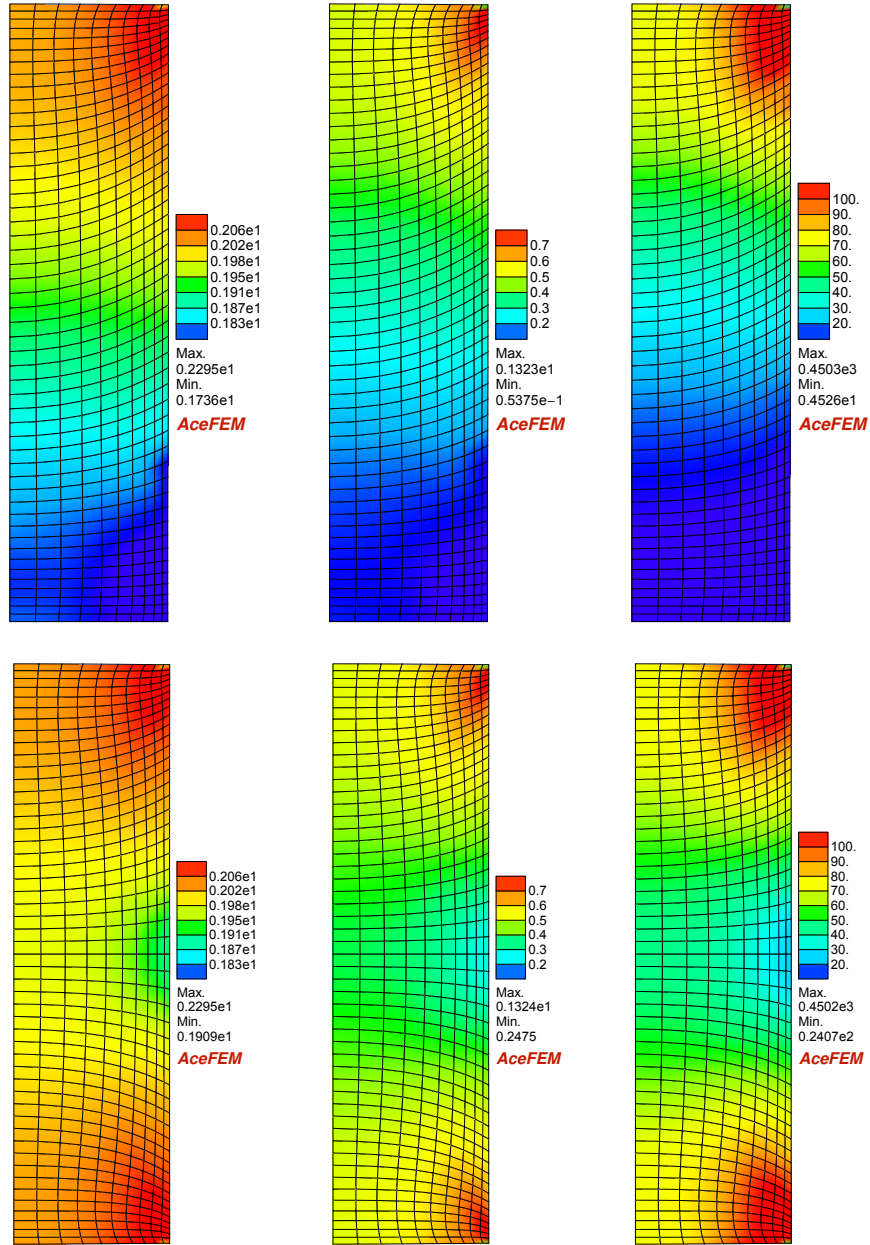


Figure 6: Distribution of density  $\rho$  (in g/cm<sup>3</sup>, left), cohesion  $c$  (in MPa, centre), tangent elastic bulk modulus  $K_t$  (in MPa, right) for single action compression (top row) and double action compression (bottom row) of alumina powder (wall/powder and punch/powder friction coefficient was assumed equal to 0.4).

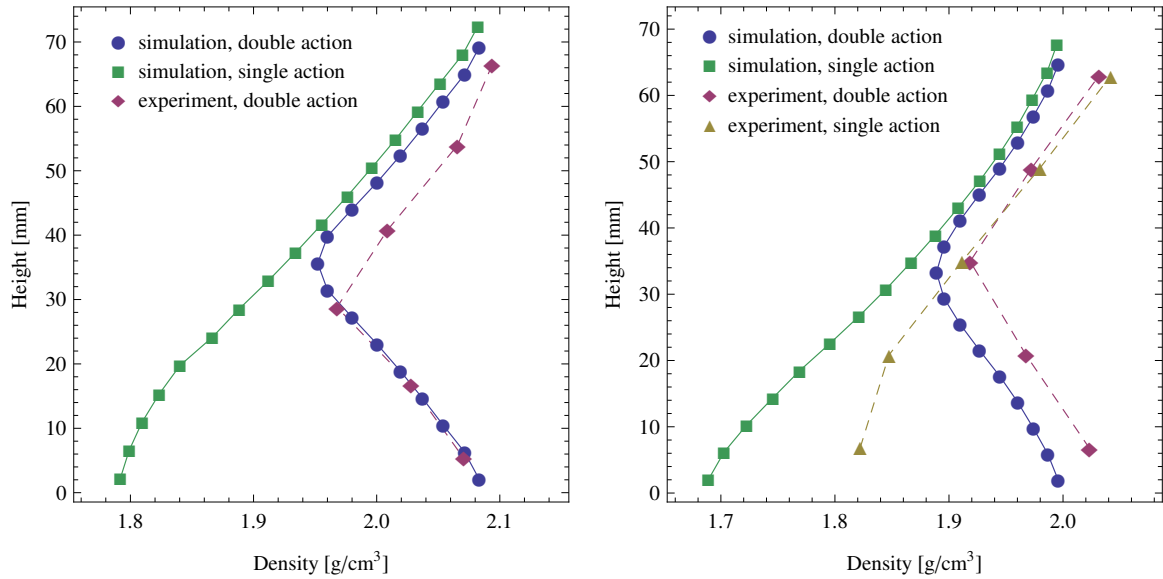


Figure 7: Density distribution for single and double action compression in a mould with friction at the wall: alumina (left) and aluminum silicate (right) powder. Experimental results are also included.

### 3.3 Forming in a mould with a cross-shaped punch

To induce large inhomogeneities during cold forming of a sample, we have designed and manufactured a (30 mm diameter) cross-shaped punch with 2.5 mm deep grooves, shown in Fig. 8, where the quotes are in mm.

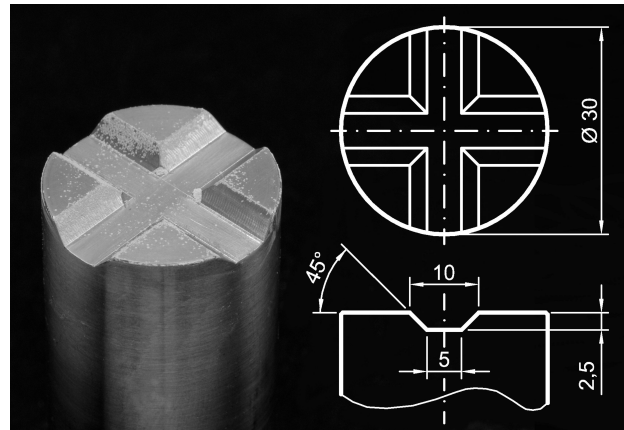


Figure 8: The cross-shaped punch (quotes are in mm) used to form the pieces shown in Fig. 9.

The punch has been used to form pieces from 8 g of alumina powder at a vertical load of 70 kN, see Fig. 9. As a consequence of the highly inhomogeneous density distribution obtained with the cross-shaped punch, the sample sometimes breaks after mold ejection, see upper part of Fig. 9.



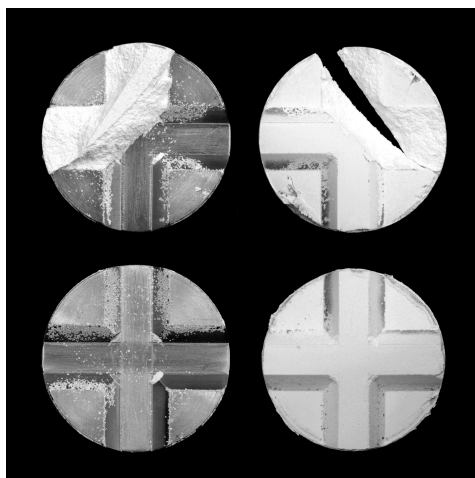


Figure 9: Cross-shaped (30 mm diameter) punch (left) and the formed pieces (right), broken (upper part) and intact (lower part) after ejection.

By exploiting the symmetry of the punch, only one quarter of the specimen has been modelled in order to reduce the computation time. Simplified boundary conditions are applied as described below. The loading is applied by prescribing the vertical displacement at the top surface, while the horizontal displacements at the top surface are fully constrained. At the bottom surface, all displacements are constrained. This corresponds to high friction and sticking contact at the top and the bottom surfaces. The horizontal displacements are constrained on the lateral surface which approximately corresponds to frictionless contact at the mould surface. Considering that the aspect ratio of the specimen is low, friction at the mould surface is expected to have a small influence on the forming force and on the deformation pattern.

Unloading and spring-back are modelled in two steps. In the first step, the reaction forces at the top and bottom surfaces are gradually decreased to zero to simulate unloading of the punch. In the second step, the reaction forces at the lateral surface are gradually decreased to zero to simulate ejection from the mould. Note that both steps are accompanied by plastic deformations induced by specimen inhomogeneity and the associated residual stresses.

The undeformed and deformed meshes employed for the simulations are shown in Fig. 10, while density and cohesion distribution, spring-back displacements and residual stresses are shown in Figs. 11–13. Inhomogeneity of the microstructure of the formed piece is clearly visible in Fig. 11 which results in nonuniform deformation during unloading and spring-back (Fig. 12) and significant residual stresses after unloading (Fig. 13).

The effect of plastic deformations that accompany spring-back is illustrated in Fig. 14, showing the distribution of the associated increment of cohesion  $\Delta c$ . There is a decrease of cohesion (so that the increment is negative) localized near the edge of the grooves, which is connected to a plastic softening that may lead to damage of the piece, as indeed observed in experiment, see upper part of Fig. 9. Softening during spring-back may also be responsible for the mesh-dependent oscillations of residual stresses, as seen in Fig. 13. Such features of the stress field are not observed during the loading stage.

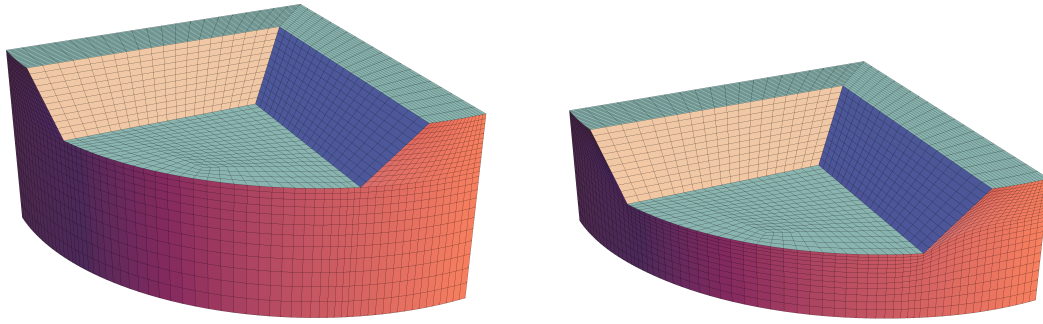


Figure 10: Finite element mesh (one quarter) for the cross-shaped specimen: undeformed (left) and deformed (right).

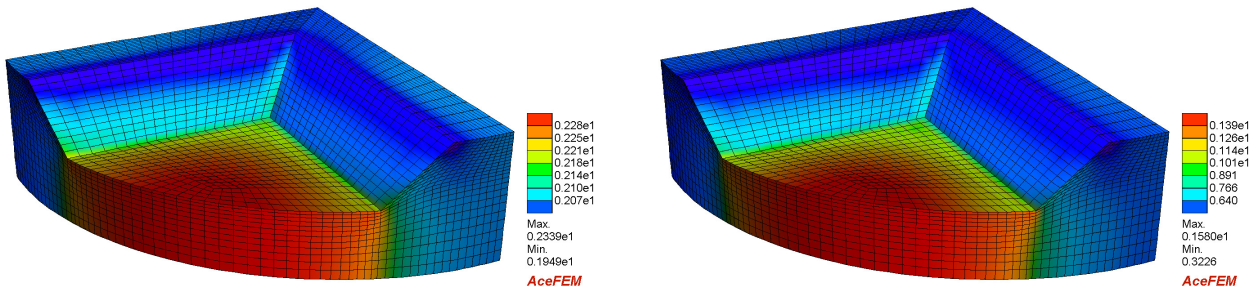


Figure 11: Simulated distributions of density  $\rho$  (in  $\text{g/cm}^3$ , left) and cohesion  $c$  (in MPa, right) within the cross-shaped specimen.

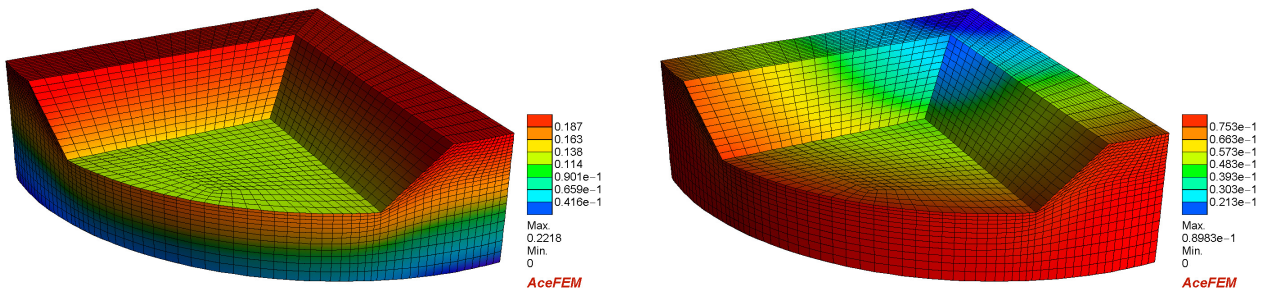


Figure 12: Simulated spring-back displacement components (in mm) within the cross-shaped specimen: axial (left) and radial (right).

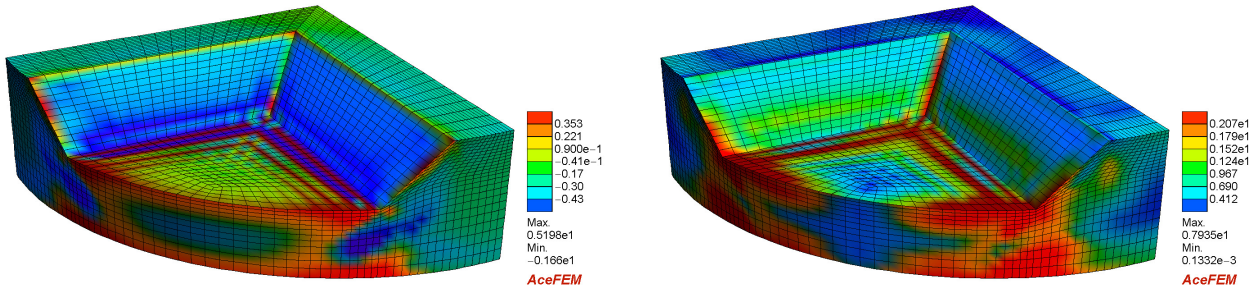


Figure 13: Simulated distributions of residual stresses (in MPa) within the cross-shaped specimen after spring-back: mean stress  $p$  (left) and deviatoric invariant  $q$  (right).

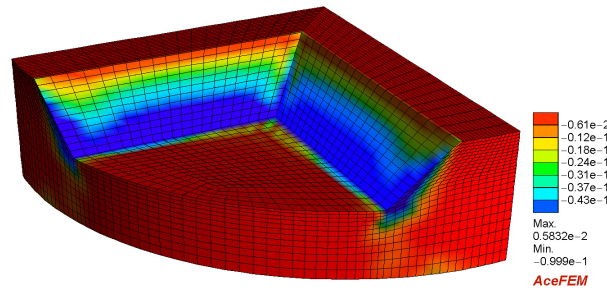


Figure 14: Simulated map of change in cohesion  $\Delta c$  (in MPa) after spring-back for the cross-shaped specimen. Note the strong decrease near the edge of the grooves.

Finally the simulated force versus displacement relation during forming of the cross-shaped sample has been compared to the experimental values in Fig. 15 for the small and large strain cases.

The predictive capabilities of the model, particularly in the large strain version, are evident from this figure. It is reminded here that the two models predict a very similar response for uniform compression. The discrepancy between the two models, which is clearly visible in Fig. 15, is thus associated with non-uniform deformation within the specimen. The configuration changes during powder forming are large, and, as expected, the finite deformation effects are significant.

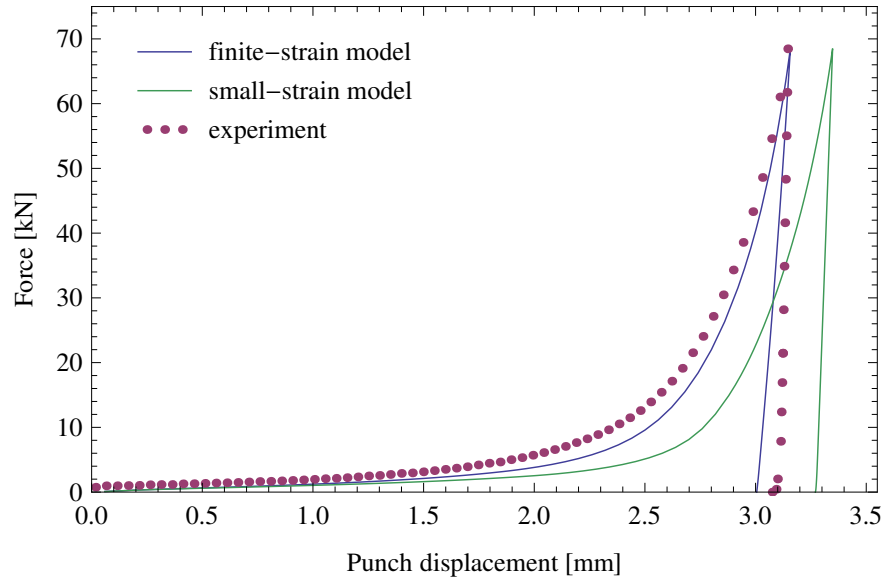


Figure 15: Simulated (small and large strain analyses) force-displacement curve for the forming of the cross-shaped specimen, compared to experimental results.

## 4 Conclusions

It has been shown that a constitutive model capable of describing compaction of ceramic powders and based on the concept of elastoplastic coupling can be implemented in an efficient way, both in a small strain and a large strain version, and can be coupled with Coulomb friction at the mould/powder interface. This model allows the simulation of ceramic forming processes and the correct prediction of the spring-back after mould ejection and of the distributions in the green body of: (i.) density, (ii.) cohesion, (iii.) elastic parameters, and (iv.) residual stress. Therefore, the developed constitutive model can become an effective tool for design of ceramic pieces.

*Acknowledgments* Financial support from the European FP7 - Intercer2 project (PIAP-GA-2011-286110-INTERCER2) is gratefully acknowledged.

## References

- [1] Ahzi, S., Asaro, R.J., Parks, D.M., 1993. Application of crystal plasticity theory for mechanically processed BSCCO superconductors. *Mech. Mater.* 15, 201222.
- [2] Alart P., Curnier A. 1991. A mixed formulation for frictional contact problems prone to Newton like solution methods. *Comp. Meth. Appl. Mech. Eng.* 92, 353-375.
- [3] Ariffin, A.K., Gethin, D.T., Lewis, R.W., 1998. Finite element simulation and experimental validation for multilevel powder compact. *Powder Metall.* 41, 189197.

- [4] Aydin, I., Briscoe, B.J., Sanliturk, K.Y., 1997a. Dimensional variation of die-pressed ceramic green compacts: comparison of a finite element modelling with experiment. *J. Eur. Ceram. Soc.* 17, 12011212.
- [5] Aydin, I., Briscoe, B.J., Ozkan, N., 1997b. Modeling of powder compaction: a review. *MRS Bull.* 22, 4551.
- [6] Balakrishnan, A., Martin, C.L., Saha, B.P. and Joshi, S. 2011. Modelling of compaction and green strength of aggregated ceramic powders. *J. Am. Ceram. Soc.* 94, 1046-1052.
- [7] Baklouti, S., Chartier, T., Gault, C., Baumard, J.F. 1997. The Effect of Binders on the Strength and Young's Modulus of Dry Pressed Alumina. *J. Europ. Ceramic Soc.* 18, 323-328.
- [8] Baklouti, S., Chartier, T., Gault, C., Baumard, J.F. 1999. Young's Modulus of Dry-pressed Ceramics: The Effect of the Binder. *J. Europ. Ceramic Soc.* 19, 1569-1574.
- [9] Bigoni, D. 2012. *Nonlinear Solid Mechanics. Bifurcation theory and material instability*, Cambridge University Press.
- [10] Bigoni, D. and Piccolroaz, A. 2004. Yield criteria for quasibrittle and frictional materials. *Int. J. Solids Struct.*, 41, 2855-2878.
- [11] Bosi, F., A. Piccolroaz, M. Gei, F. Dal Corso, A. Cocquio and Bigoni, D. 2013. Experimental investigation of the elastoplastic response of aluminum silicate spray-dried powder during cold compaction. *J. Europ. Ceramic Soc.* Submitted.
- [12] Brandt, J., Nilsson, L., 1998. FE-simulation of compaction and solid-state sintering of cemented carbides. *Mech. Cohesive-Frict. Mater.* 3, 181205.
- [13] Brandt, J., Nilsson, L., 1999. A constitutive model for compaction of granular media, with account for deformation induced anisotropy. *Mech. Cohesive-Frict. Mater.* 4, 391418.
- [14] Brannon, R.M. and Leelavanichkul, S. (2010) Received: A multi-stage return algorithm for solving the classical damage component of constitutive models for rocks, ceramics, and other rock-like media. *Int. J. Fracture* 163, 133149.
- [15] Carneim, T.J., Green, D.J. 2001. Mechanical Properties of Dry-Pressed Alumina Green Bodies. *J. Am. Ceram. Soc.*, 84, 14051410.
- [16] Cooper, A.R., Eaton, L.E., 1962. Compaction behavior of several ceramic powders. *J. Am. Ceram. Soc.* 45, 97101.
- [17] Dougill, J.W., 1976. On stable progressively fracturing solids. *Z. Angew. Math. Phys.* 27, 423437.
- [18] Ewsuk, K.G., Argüello, J.G., Zeuch, D.H., Farber, B., Carinci, L., Kaniuk, J., Keller, J., Cloutier, C., Gold, B., Cass, R.B., French, J.D., Dinger, B., Blumenthal, W., 2001a. CRADA develops model for powder pressing and die design, Part one. *Am. Ceram. Soc. Bull.* 80, 5360.
- [19] Ewsuk, K.G., Argüello, J.G., Zeuch, D.H., Farber, B., Carinci, L., Kaniuk, J., Keller, J., Cloutier, C., Gold, B., Cass, R.B., French, J.D., Dinger, B., Blumenthal, W., 2001b. CRADA develops model for powder pressing and die design, Part two. *Am. Ceram. Soc. Bull.* 80, 4146.

- [20] Gu, Y., Henderson, R.J., and Chandler, H.W. 2006. Visualizing isostatic pressing of ceramic powders using finite element analysis. *J. Europ. Ceramic Soc.* 26, 2265-2272.
- [21] Henderson, R.J., Chandler, H.W., Akisanya, A.R., Barber, H. and Moriarty, B. 2000. Finite element modelling of cold isostatic pressing. *J. Europ. Ceramic Soc.* 20, 1121-1128.
- [22] Hueckel, T., 1975. On plastic flow of granular and rock-like materials with variable elasticity moduli. *Bull. Pol. Acad. Sci., Ser. Techn.* 23, 405414.
- [23] Hueckel, T., 1976. Coupling of elastic and plastic deformation of bulk solids. *Meccanica* 11, 227235.
- [24] Keller, J.M., French, J.D., Dinger, B., McDonough, M., Gold, B., Cloutier, C., Carinci, L., Van Horn, E., Ewsuk, K., Blumenthal, B., 1998. Industry, government team to improve ceramic manufacturing. *Am. Ceram. Soc. Bull.* 77, 5257.
- [25] Kim, H.G., Gillia, O., Dorémus, P., Bouvard, D., 2002. Near net shape processing of a sintered alumina component: adjustment of pressing parameters through finite element simulation. *Int. J. Mech. Sci.* 44, 25232539.
- [26] Kim, H.G., Lee, H.M., Kim, K.T. 2001. Near-net-shape forming of ceramic powder under cold combination pressing and pressureless sintering. *J. Eng. Mat. Tech.* 123, 221-228.
- [27] Korelc, J., 2002. Multi-language and multi-environment generation of nonlinear finite element codes. *Engineering with Computers*, 18, 312327.
- [28] Korelc, J., 2009. Automation of primal and sensitivity analysis of transient coupled problems. *Comp. Mech.*, 44, 631649.
- [29] Kounga Njiwa, A.B., Aulbach, E., Rödel, J. 2006. Mechanical Properties of Dry-Pressed Powder Compacts: Case Study on Alumina Nanoparticles. *J. Am. Ceram. Soc.*, 89, 26412644.
- [30] Lee, S.C., Kim, K.T. 2008. Densification behaviour of nanocrystalline titania powder under cold compaction. *Powder Tech.* 186, 99-106.
- [31] Lengiewicz, J., Korelc, J., Stupkiewicz, S. 2011. Automation of finite element formulations for large deformation contact problems. *Int. J. Num. Meth. Eng.* 85, 1252-1279.
- [32] Park, H., Kim, K.T. 2001. Consolidation behaviour of SiC powder under cold compaction. *Mat. Sci. Eng. A* 299, 116-124.
- [33] Penasa, M., Piccolroaz, A., Argani, L. and Bigoni, D. 2013. Integration algorithms of elastoplasticity for ceramic powder compaction. *J. Europ. Ceramic Soc.* Submitted.
- [34] Piccolroaz, A., Bigoni, D., 2009. Yield criteria for quasibrittle and frictional materials: a generalization to surfaces with corners. *Int. J. Solids Struct.*, 46, 3587-3596.
- [35] Piccolroaz, A., Bigoni, D., Gajo, A. 2006a. An elastoplastic framework for granular materials becoming cohesive through mechanical densification. Part I - small strain formulation. *Europ. J. Mech. A: Solids*, 25, 334-357.
- [36] Piccolroaz, A., Bigoni, D., Gajo, A. 2006b. An elastoplastic framework for granular materials becoming cohesive through mechanical densification. Part II - the formulation of elastoplastic coupling at large strain. *Europ. J. Mech. A: Solids*, 25, 358-369.

- [37] Piccolroaz, A., Penasa, M., Argani, L., Bigoni, D. 2013. Integration algorithms of elastoplasticity for ceramic powder compaction. Submitted.
- [38] Stupkiewicz, S., Denzer, R.P., Piccolroaz, A., Bigoni, D. 2013. Implicit yield function formulation for granular and rock-like materials. Submitted.
- [39] Zeuch, D.H., Grazier, J.M., Argüello, J.G., Ewsuk, K.G., 2001. Mechanical properties and shear failure surfaces for two alumina powders in triaxial compression. *J. Mater. Sci.* 36, 29112924.
- [40] Zipse, H., 1997. Finite-element simulation of die pressing and sintering of a ceramic component. *J. Eur. Ceram. Soc.* 17, 17071713.